

# Calibration, inversion and sensitivity analysis for hydro-morphodynamic models through the application of adjoint methods

Mariana C. A. Clare<sup>a,\*</sup>, Stephan C. Kramer<sup>a</sup>, Colin J. Cotter<sup>b</sup> and Matthew D. Piggott<sup>a</sup>

<sup>a</sup>Department of Earth Science and Engineering, Imperial College London, UK.

<sup>b</sup>Department of Mathematics, Imperial College London, UK.

---

## ARTICLE INFO

### Keywords:

adjoint methods  
uncertainty  
sediment transport  
morphology  
tsunami inversion  
model calibration

## ABSTRACT

The development of reliable, sophisticated hydro-morphodynamic models is essential for protecting the coastal environment against hazards such as flooding and erosion. There exists a high degree of uncertainty associated with the application of these models, in part due to incomplete knowledge of various physical, empirical and numerical closure related parameters in both the hydrodynamic and morphodynamic solvers. This uncertainty can be addressed through the application of adjoint methods. These have the notable advantage that the number and/or dimension of the uncertain parameters has almost no effect on the computational cost associated with calculating the model sensitivities.

Here, we develop the first freely available and fully flexible adjoint hydro-morphodynamic model framework. This flexibility is achieved through using the *pyadjoint* library, which allows us to assess the uncertainty of any parameter with respect to any output functional, without further code implementation. The model is developed within the coastal ocean model *Thetis* constructed using the finite element code-generation library *Firedrake*. We present examples of how this framework can perform sensitivity analysis, inversion and calibration for a range of uncertain parameters based on the final bedlevel. These results are verified using so-called dual-twin experiments, where the ‘correct’ parameter value is used in the generation of synthetic model test data, but is unknown to the model in subsequent testing. Moreover, we show that inversion and calibration with experimental data using our framework produces physically sensible optimum parameters and that these parameters always lead to more accurate results. In particular, we demonstrate how our adjoint framework can be applied to a tsunami-like event to invert for the tsunami wave from sediment deposits.

---

**This manuscript is a non-peer reviewed EarthArXiv preprint that has been submitted for publication in Computers & Geosciences**

---

## 1. Introduction

Hydro-morphodynamic models are highly complex coupled models used to simulate hydrodynamics, sediment transport and bed morphology in both fluvial and coastal environments. They are often associated with a high degree of uncertainty in part due to incomplete knowledge of various physical, empirical and numerical closure related parameters in both the hydrodynamic and morphodynamic solvers.

Research on methods to assess this uncertainty is ongoing. A range of statistical methods has been applied to hydro-morphodynamic models, including Monte Carlo methods (e.g. Villaret et al., 2016; Hieu et al., 2006; Kopmann et al., 2012) and ensemble methods (e.g. Unguendoli, 2018; Tang et al., 2018). Both of these require multiple runs of very computationally expensive models to produce statistically robust results, e.g. Harris et al. (2018) require 240,000 runs of the complex hydro-morphodynamic model XBeach. This makes these methods often computationally unfeasible, particularly when simulating the long time periods required in many hydro-morphodynamic problems, and means that simplified models must be used: e.g. in Dissanayake et al. (2014), a 1D rather than 2D model is used.

Other advanced numerical methods can be used to assess uncertainty. For example, a tangent linear approach has been implemented with the hydro-morphodynamic model Telemac-Mascaret (Hervouet, 1999). This implementation

---

✉ [m.clare17@imperial.ac.uk](mailto:m.clare17@imperial.ac.uk) (M.C.A. Clare)

ORCID(s): 0000-0002-5010-0363 (M.C.A. Clare); 0000-0002-9193-5092 (S.C. Kramer); 0000-0001-7962-8324 (C.J. Cotter); 0000-0002-7526-6853 (M.D. Piggott)

is presented in Naumann and Riehme (2008) and examples of its application in morphodynamic test cases are given in Kopmann et al. (2012); Villaret et al. (2016); Hieu et al. (2006); Dalledonne et al. (2017); Riehme et al. (2010). This first order method is computationally cheaper than statistical methods, but must be run at least once for each uncertain parameter of interest. This can become computationally expensive because Villaret et al. (2016) state that each tangent linear model run in their implementation takes approximately three times more than a forward model run (*i.e.* a standard hydro-morphodynamic model run).

In this work, we use adjoint methods to assess model uncertainty to great advantage. Adjoint methods are used in numerical modelling to compute gradients of model outputs with respect to input parameters. Thus, they are a useful tool for sensitivity analysis and for the calibration and inversion of uncertain parameter values. Their main advantage is that only one adjoint evaluation is required to compute the sensitivity of an output quantity irrespective of the number of uncertain parameters, or their dimension (e.g. a scalar or a field of values). Therefore, any number of multi-dimensional uncertain parameters can be considered at the same time with almost no effect on the computational cost (see e.g. Funke et al. (2017); Chen et al. (2014); Heemink et al. (2002) where adjoint methods are applied to hydrodynamic models).

Adjoint methods have already been successfully applied to hydro-morphodynamic models for non-cohesive sediments, although not to a fully coupled 2D hydro-morphodynamic model. For example, they are applied to a simple 1D hydro-morphodynamic model for turbidity currents in Parkinson et al. (2017) and to the morphodynamic component *Sisyphé* of Telemac-Mascaret in Kopmann et al. (2012); Merkel et al. (2013, 2016). However, only three published test cases use the adjoint method with *Sisyphé* and recent research appears to be limited. Additionally, to the best of our knowledge, adjoint methods have never been applied to the fully coupled hydro-morphodynamic model in Telemac-Mascaret. This is significant because many parameters influence both the hydrodynamic and morphodynamic components and there are many feedback effects between these two components. Thus, only calculating the adjoint on the morphodynamic component reduces the accuracy of the results of the adjoint methods and limits the cases where they can be applied. Furthermore, the implementation of the adjoint method within the Telemac-Mascaret model is financially expensive because it requires the use of a commercial NAG FORTRAN compiler (see Merkel et al., 2016).

There is thus a clear need for the fully flexible, free-to-use, and relatively computationally cheap adjoint framework that we present in this work. This flexibility is achieved by using the *pyadjoint* (Farrell et al., 2013) library, which works with the code-generation framework *Firedrake* (Rathgeber et al., 2017) to automatically derive adjoint equations using the high level abstraction of the finite element equations available within all *Firedrake* based models. Thus, we can assess the uncertainty of any parameter in the model with respect to any output functional, without further code implementation. A further advantage of using *pyadjoint* is that, for all test cases considered in this work, an adjoint run takes at most three times more than a forward model run. This can be contrasted with Telemac-Mascaret, where for the test case in Merkel et al. (2016), the adjoint run is 135 times more computationally expensive than the forward model run.

In this work, in order to benefit fully from this *Firedrake - pyadjoint* framework, we use the 2D depth-averaged non-cohesive coupled hydro-morphodynamic model presented in Clare et al. (2021a), which has been developed using *Firedrake* within the finite element coastal ocean modelling system *Thetis* (Kärnä et al., 2018). Although the adjoint method has previously been used with the hydrodynamic component of *Thetis*, e.g. in Warder et al. (2021), this work is the first time *pyadjoint* is used in a coupled model. A further advantage of this hydro-morphodynamic model is that it is more accurate than industry-standard models such as Telemac-Mascaret, as shown in Clare et al. (2021a), partly because of the relatively novel use of a discontinuous Galerkin based finite element discretisation. This has several advantages, as discussed in Clare et al. (2021a), including being well-suited for advection-dominated problems such as those considered in this work (Kärnä et al., 2018).

The remainder of this paper is structured as follows: Section 2 describes the adjoint method; Section 3 outlines the hydro-morphodynamic model; in Sections 5 and 4 uses simple test cases to show how adjoint methods can be used for sensitivity analysis and to perform inversion and calibration; Section 6 shows how adjoint methods can be used to invert for tsunami-like waves from sediment deposits and, finally, Section 7 presents some concluding remarks.

## 2. Adjoint methods

Adjoint methods can compute the gradient of a model output functional with respect to a set of parameters and are thus useful for assessing uncertainty (Farrell et al., 2013). To establish notation, we first briefly present a derivation of these methods, following Funke (2012) and Funke et al. (2017).

The hydro-morphodynamic forward model to be presented in Section 3 can be written in the abstract form  $F(u, \mathbf{m}) = 0$  where  $\mathbf{m}$  is a set of uncertain parameters and  $u$  is the model solution. Any given output functional,  $J$ , depends only on  $\mathbf{m}$  and  $u$  and thus

$$\frac{dJ}{d\mathbf{m}} = \frac{\partial J}{\partial u} \frac{du}{d\mathbf{m}} + \frac{\partial J}{\partial \mathbf{m}}. \quad (1)$$

Differentiating the forward model with respect to  $\mathbf{m}$  yields

$$\frac{du}{d\mathbf{m}} = - \left( \frac{\partial F}{\partial u} \right)^{-1} \frac{\partial F}{\partial \mathbf{m}}, \quad (2)$$

and therefore

$$\frac{dJ}{d\mathbf{m}} = - \frac{\partial J}{\partial u} \left( \frac{\partial F}{\partial u} \right)^{-1} \frac{\partial F}{\partial \mathbf{m}} + \frac{\partial J}{\partial \mathbf{m}}, \quad (3)$$

which can be evaluated using either the adjoint or the tangent linear approach. If adjoint methods are used, we evaluate  $\lambda$  in

$$\lambda = \frac{\partial J}{\partial u} \left( \frac{\partial F}{\partial u} \right)^{-1}, \quad (4)$$

and substitute it into

$$\frac{dJ}{d\mathbf{m}} = -\lambda \frac{\partial F}{\partial \mathbf{m}} + \frac{\partial J}{\partial \mathbf{m}}, \quad (5)$$

to find the derivative. Note, only one linear solve is ever necessary to evaluate (4), independent of the number of uncertain parameters or their dimension.

If the tangent linear approach is used, we evaluate  $\mu$  in

$$\mu^T = - \left( \frac{\partial F}{\partial u} \right)^{-1} \frac{\partial F}{\partial \mathbf{m}}. \quad (6)$$

and substitute it into

$$\frac{dJ}{d\mathbf{m}} = \frac{\partial J}{\partial u} \mu^T + \frac{\partial J}{\partial \mathbf{m}}, \quad (7)$$

to find the derivative. Note this is equivalent to (2), meaning that the tangent linear approach is solving for  $du/d\mathbf{m}$ . The expression for  $\mu$  can be solved using a variety of different methods including explicitly inverting the linearised PDE operator  $\partial F/\partial u$  or performing an iterative solve for each dimension of  $\mathbf{m}$  (see Funke, 2012). For all methods, the computational cost of solving this expression scales linearly with the dimension of  $\mathbf{m}$ . By contrast, once  $\mu$  is computed, then the derivative of the output functional  $J$  can be efficiently computed for multiple different outputs. This makes the tangent linear approach well-suited to problems with a relatively small number of uncertain one-dimensional input parameters but a large number of uncertain outputs and/or an output functional which is a spatially-varying field. Conversely, the adjoint solution is ideally suited to problems where there are multiple uncertain input parameters (both scalar and multi-dimensional), which is the case for hydro-morphodynamic problems.

Adjoint methods can be difficult to derive and implement, but we overcome this problem by using the hydro-morphodynamic model from Clare et al. (2021a), which is built within *Thetis*, a *Firedrake*-based model. This means we can use the *pyadjoint* library (Farrell et al., 2013), which is constructed to work within the *Firedrake* environment. This library automatically derives the adjoint equations by first ‘taping’ (recording the sequence of numerical operations) a forward model run and then using this tape to construct the discretised adjoint equations. This means that the actual derivative of the discrete model is used (up to numerical truncation errors and solver tolerances), rather than a discrete approximation of a continuous derivative (see Funke et al., 2017). A similar methodology can also be used to implement the tangent linear approach in *pyadjoint*.

The adjoint method has already been used successfully with the hydrodynamic component of *Thetis* (e.g. Warder

et al., 2021), but we expand upon this here by using the adjoint method with a coupled model which requires extending the *pyadjoint* code to ensure that the coupling is correctly captured. In particular, the coupling between the components of the hydro-morphodynamic model relies on a split mechanism, which extracts the velocity and elevation from the hydrodynamic component so that both can be passed to the morphodynamic component. The new *pyadjoint* code tapes and calculates the adjoint of this operation, thus facilitating the use of *pyadjoint* for all *Firedrake*-based coupled models (full details of the code change are given in *Firedrake Project* (2021)). In this work, we do not show the adjoint equations since using *pyadjoint* means we do not have to manually derive them. However, for the interested reader, Funke (2012) shows the derivation of the adjoint form of the shallow water equations, and the adjoint of the sediment concentration equation and Exner equation can be derived following a similar methodology.

The Taylor remainder convergence test (explained in more detail in Funke (2012)) can be used to verify the adjoint implementation derived by *pyadjoint* and in particular the new adjoint implementation of our coupled model. This test checks whether the gradient  $\frac{dJ}{d\mathbf{m}}$  derived using the adjoint solution is correct by verifying that the Taylor residual converges at second order

$$|J(\mathbf{m} + h\delta\mathbf{m}) - J(\mathbf{m}) - h\delta\mathbf{m}\frac{dJ}{d\mathbf{m}}| = \mathcal{O}(h^2) \quad \text{as } h \rightarrow 0, \quad (8)$$

where  $\delta\mathbf{m}$  is a random perturbation. This second-order convergence is very sensitive to implementation errors (see Funke, 2012) and thus represents a strict code verification check. All test cases outlined in this work pass it, confirming that the adjoint implementation of our coupled hydro-morphodynamic model is correct.

## 2.1. Using adjoint methods to address uncertainty

Adjoint methods can be used to address the uncertainty of hydro-morphodynamic models with respect to particular parameters, through sensitivity analysis and calibration and inversion. Note we perform calibration by inverting our model for the uncertain parameters and using an optimisation algorithm to minimise the error between the model output and the desired output to improve model accuracy. Thus calibration can be seen as a sub-type of inversion and we use the same methodology for both.

To analyse the sensitivity of model outputs to particular uncertain parameters, we use adjoint methods to compute the derivative  $dJ/d\mathbf{m}$ . This output functional,  $J$ , can take many forms and here we use

$$J(\mathbf{u}^{\text{model}}, \mathbf{m}) := \frac{1}{2} \sum_{j=1}^{N_{\text{out}}} \int_0^T \int_{\Omega} \sqrt{|u_j^{\text{model}}|^2 + \epsilon} \, dx \, dt, \quad (9)$$

which analyses the sensitivity of an integrated output to uncertain parameters (in Section 4.2, this output is chosen to be the bedlevel). Here  $\Omega$  is the domain of the model,  $N_{\text{out}}$  the number of output variables used and  $\epsilon$  is a parameter set to  $10^{-6}$  which we have added to smooth our results if  $u_j^{\text{model}} = 0$  anywhere in the domain.

For inversion and calibration, we minimise the following problem using the default L-BFGS-B algorithm available via the SciPy library (Jones et al., 2001)

$$\begin{aligned} & \underset{u, \mathbf{m}}{\text{minimize}} && J(u, \mathbf{m}) \\ & \text{subject to} && F(u, \mathbf{m}) = 0. \end{aligned} \quad (10)$$

The general form of the output functional  $J$  is

$$J(\mathbf{u}^{\text{model}}, \mathbf{m}) := \alpha \sum_{j=1}^{N_{\text{out}}} \int_0^T \int_{\Omega} |u_j^{\text{true}} - u_j^{\text{model}}|^2 \, dx \, dt + \sum_{i=1}^{N_{\text{in}}} \beta_i \int_0^T \int_{\Omega} |m_i|^2 \, dx \, dt, \quad (11)$$

where  $N_{\text{in}}$  is the number of uncertain parameters and  $\alpha$  is a user-specified scaling factor. The first integral term in (11) is the difference between the model output and the true value, either experimental/real-world data or, in the case of a dual twin experiment, synthetic data generated using a previous run of the model with known parameter values. Unlike with (9), we do not use a square root in the term, so as to more severely penalise large differences between

the model and true values. The second integral term is a Tikhonov regularisation term, which aids in the solution of ill-posed problems and can be used to prevent the magnitude of the parameters becoming unphysical (see Engl et al., 1996). The amount of regularisation is controlled by  $\beta_i$  and can be different for each uncertain parameter.

### 3. Hydro-morphodynamic model

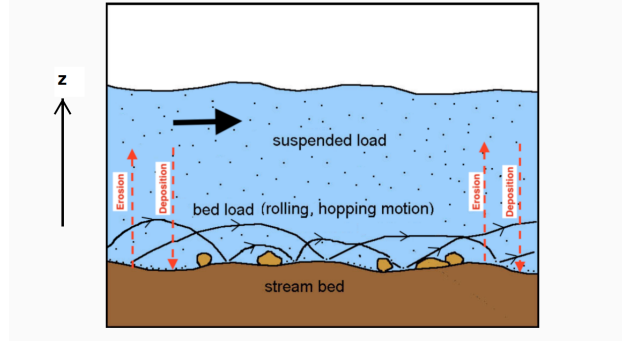


**Figure 1:** Diagram of sediment transport. Source: Clare et al. (2021b).

We now briefly describe the 2D depth-averaged coupled hydro-morphodynamic model presented in Clare et al. (2021a) and used in this work. It is able to update the bed morphology as a result of both suspended sediment and bedload transport, while taking into account gravitational and helical flow effects. Figure 1 shows a diagrammatic representation of what our hydro-morphodynamic model simulates.

For reasons of stability, the time derivatives in the model equations are approximated using a fully-implicit backward Euler timestepping scheme. Clare et al. (2021a) give full details on the original development of this model for a fully wet domain which is used in the test cases in Section 4 and 5 and the equations are summarised below:

#### Shallow water equations

$$\frac{\partial h}{\partial t} + \nabla \cdot (h\mathbf{U}) = 0, \quad (12)$$

$$\frac{\partial \mathbf{U}}{\partial t} + \mathbf{U} \cdot \nabla \mathbf{U} + \mathbf{g} \nabla \eta = \nu \nabla^2 \mathbf{U} - \frac{C_h}{h} \|\mathbf{U}\| \mathbf{U}, \quad (13)$$

where  $h$  is the total depth,  $\mathbf{U}$  the depth-averaged velocity,  $\eta$  the free surface elevation,  $\mathbf{g}$  the gravitational constant,  $\nu$  the viscosity parameter and  $C_h$  the quadratic drag coefficient;

#### Non-conservative sediment concentration equation

$$\frac{\partial C}{\partial t} + F_{\text{corr}} \mathbf{U} \cdot \nabla C = \epsilon_s \nabla^2 C + \frac{E_b - D_b}{h}, \quad (14)$$

where  $C$  is the depth-averaged sediment concentration,  $\epsilon_s$  the diffusivity coefficient,  $E_b$  the erosion flux,  $D_b$  the deposition flux, and  $F_{\text{corr}}$  a correction factor;

#### Exner equation

$$\frac{(1-p')}{m_f} \frac{\partial z_b}{\partial t} + \nabla \cdot \mathbf{Q}_b = D_b - E_b, \quad (15)$$

where  $m_f$  is a morphological acceleration factor,  $p'$  the porosity,  $\mathbf{Q}_b$  the bedload transport and  $z_b$  the bedlevel (also known as the bathymetry). Note, throughout  $z_b$  is defined such that the water depth,  $h = \eta - z_b$ .

Here,  $F_{\text{corr}}$  in (14) accounts for the fact that depth-averaging the product of two variables is not equivalent to multiplying two depth-averaged variables; and the morphological acceleration factor,  $m_f$ , in (15) artificially increases

the rate of bedlevel changes compared with the underlying hydrodynamics, thus decreasing computational cost. See Clare et al. (2021a) for more details on these parameters.

### 3.1. Wetting-and-drying

Coastal zone test cases (like that considered in Section 6) often have a wetting-and-drying interface. Thus, Clare et al. (2021b) extends the hydro-morphodynamic model in Clare et al. (2021a) to deal with wet-dry domains by using the wetting-and-drying scheme detailed in Kärnä et al. (2011), where the depth,  $h$ , is replaced by

$$\tilde{H} := \eta - z_b + \frac{1}{2} \left( \sqrt{h^2 + \delta^2} - h \right), \quad (16)$$

where  $\delta$  is a user-defined parameter set to be approximately equal to  $d \|\nabla h\|$  with  $d$  the mesh length scale. To avoid the sediment leakage that is observed when applying (14) in combination with wetting-and-drying, in the wetting-and-drying model we use the following conservative sediment concentration equation

$$\frac{\partial}{\partial t}(\tilde{H}C) + \nabla \cdot (F_{\text{corr}} \mathbf{U} \tilde{H}C) = \epsilon_s \nabla^2(\tilde{H}C) + E_b - D_b. \quad (17)$$

Finally, the Exner equation (15) is unchanged because it is not explicitly dependent on depth. Full details on the wetting-and-drying hydro-morphodynamic model are given in Clare et al. (2021b).

## 4. Sensitivity analysis for a Meander

As an initial test case, we consider flow around the curved channel of a meander and use the configuration from experiment 4 of Yen and Lee (1995). This test case has already been validated for our hydro-morphodynamic model in Clare et al. (2021a). Figure 2 is taken from the latter and shows good agreement between our *Thetis* model results and the experimental data for the bedlevel evolution (scaled using the initial bedlevel). Note that in all meander figures the flow is from the bottom left to the bottom right. For this test case, we use the same set-up as in Clare et al. (2021a) and refer the reader there for the parameter values used.

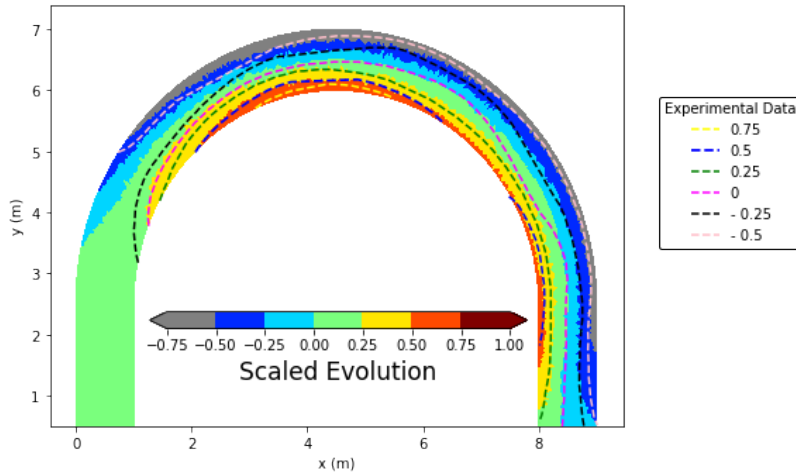


**Figure 2:** Normalised bedlevel evolution from hydro-morphodynamic model in *Thetis* with experimental data from Yen and Lee (1995) for the Meander test case. Source: Clare et al. (2021a).

### 4.1. Tangent linear approach to sensitivity analysis

This meander test case is also studied in Riehme et al. (2010), where they analyse the sensitivity of the bedlevel evolution to uncertain parameters in the hydrodynamic Telemac-2D and morphodynamic Sisyphe components of the Telemac-Mascaret model, hereafter *Sisyphe*. They use the First Order Reliability Method (FORM) to calculate the

quantity  $\sigma J_m$ , which is referred to in Riehme et al. (2010) as the standard deviation but we refer to as the scaled gradient to avoid confusion with the standard deviation of the parameter. The scaled gradient is defined as

$$\sigma J_m = \sigma_m \left. \frac{\partial J}{\partial m} \right|_{m=\langle m \rangle}, \quad (18)$$

where  $J$  is the bedlevel evolution, a spatially-varying field (*i.e.*  $J = z_b^{\text{final}} - z_b^{\text{initial}}$ ). The derivative is calculated using the tangent linear approach and  $\langle m \rangle$  and  $\sigma_m$  represent the mean and standard deviation of the uncertain parameter, respectively, which must be estimated. Note that in Riehme et al. (2010), the standard deviation  $\sigma_m$  is assumed constant and thus multiplying by  $\sigma_m$  merely scales the sensitivity without altering its spatial pattern.

Therefore, as a first verification step of our *Thetis*-pyadjoint framework, we compare the FORM analysis (18) using our model with that from using *Sisyphes* for the two scalar parameters of average sediment grain size,  $d_{50}$  and bed reference height  $k_s$ . Uncertainty quantification for these parameters is important because both are challenging to determine, particularly  $d_{50}$  which is difficult to measure in offshore environments and may change seasonally (see Jaffe et al., 2016). In addition,  $k_s$  determines the bed friction, to which hydrodynamic models are highly sensitive (see e.g. Merkel et al., 2013; Warder et al., 2021). Following Riehme et al. (2010), we assume a mean of  $1 \times 10^{-3}$  m for  $d_{50}$  and  $3 \times 10^{-3}$  m for  $k_s$ , and a standard deviation of  $1 \times 10^{-4}$  m for both.

Figure 3 shows the scaled gradient  $\sigma J_m$  of the bed evolution for the scalar parameters  $d_{50}$  and  $k_s$  computed using our model, whilst Figure 4 shows the same for *Sisyphes* taken from Riehme et al. (2010). Their comparison reveals that the distribution of the scaled gradient is consistent for both parameters. Furthermore, at the outer bend, the magnitude of the scaled gradient determined by our model is very similar to that determined by *Sisyphes* for both  $d_{50}$  and  $k_s$ . At the inner bend, however, the *Sisyphes* model predicts a greater scaled gradient magnitude for both  $d_{50}$  and  $k_s$ . These magnitude differences are to be expected because the models are constructed slightly differently and the *Thetis* final bedlevel results are more accurate than *Sisyphes*'s when compared against experimental data (see Figure 11 in Clare et al. (2021a)). Moreover, the FORM analysis with *Sisyphes* is limited because the tangent linear approach is only applied to the morphodynamic component of the model (see Riehme et al. (2010) for more details). In contrast, our *Thetis* model computes the gradient for the fully coupled hydro-morphodynamic model, hence arguably producing more accurate results.

Assessing the uncertainty of the fully coupled model to  $k_s$  is especially important because this parameter is key in determining both the sediment transport rate in the morphodynamic component and the bed friction in the hydrodynamic component. To investigate this further, we experimented with keeping  $k_s$  constant in the hydrodynamic component of our *Thetis* framework. Note this still does not make the two models set-ups identical because the  $k_s$  in the morphodynamics causes changes in the hydrodynamics not accurately captured by *Sisyphes* which then causes changes in the morphodynamics and so forth. However, this *Thetis* result agrees more closely with that from *Sisyphes*, although these results are not included here for brevity.

In summary, the spatial patterns of the scaled gradients are similar between *Thetis* and *Sisyphes* providing confidence in our *Thetis*-pyadjoint framework implementation.

## 4.2. Adjoint approach to sensitivity analysis

The tangent linear analysis above calculates the sensitivity of the bed everywhere to a single scalar parameter  $m$ . In contrast, a key advantage of using the adjoint approach is that we can determine the bed sensitivity to more than one scalar and/or to a spatially-varying parameter using a single run. In this section, we choose the latter option and analyse the sensitivity of the meander bed to the now assumed to be spatially-varying parameters  $d_{50}$  and  $k_s$ , using (9) as the integrated output functional where  $\mathbf{u}^{\text{model}}$  is the final bedlevel.

Figures 5a and 5b show the sensitivity of the bedlevel to the spatially-varying parameters  $d_{50}$  and  $k_s$ , respectively, where we have evaluated the derivative of the output functional (9) at  $d_{50} = 1 \times 10^{-3}$  m everywhere and at  $k_s = 3 \times 10^{-3}$  m everywhere, since these are the values used in the test case (see Clare et al., 2021a). Given (9) and that the meander bedlevel is centered around zero, positive sensitivity means altering the uncertain value here causes more overall bed movement compared to the unperturbed final bedlevel, and vice versa. The figures show that the most positive sensitivity region for  $k_s$  is at the centre of the channel, whereas for  $d_{50}$  it is on the left, at the flow input.

To better understand the computed sensitivities, we perturb both uncertain spatially-varying parameters from their original value in the direction of the derivative by adding their respective gradient fields (depicted in Figures 5a and 5b) multiplied by  $10^{-6}$ . We then calculate the difference between the original and perturbed final bathymetries as spatially

### Calibration, inversion and sensitivity analysis for hydro-morphodynamic models

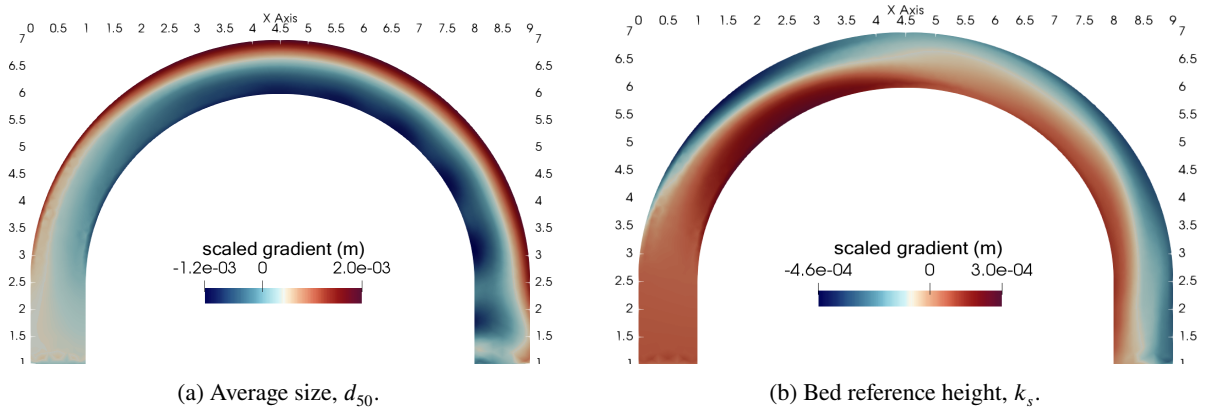


**Figure 3:** Scaled gradient of bed evolution (18) as a result of different scalar parameters using a tangent linear approach in the *Thetis*-pyadjoint framework for the Meander test case.

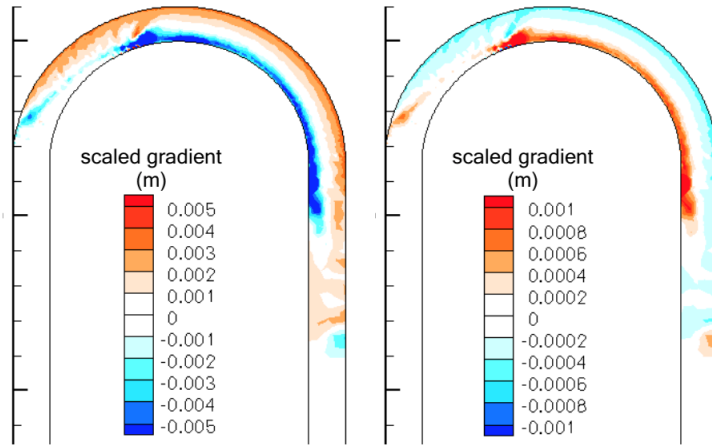


**Figure 4:** Scaled gradient of bed evolution (18) as a result of different scalar parameters using a tangent linear approach in *Sisyphé* for the Meander test case. Left:  $d_{50}$ ; Right:  $k_s$ . Source: Riehme et al. (2010).

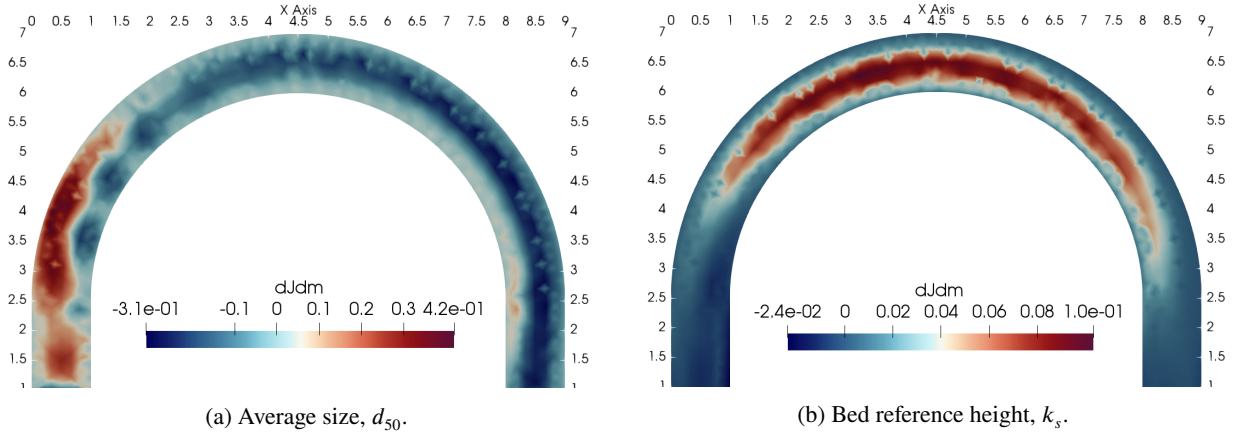
varying fields. Note that a positive value indicates that perturbing the uncertain value results in more deposition and a negative value that it results in more erosion.

Figure 6a shows that perturbing  $d_{50}$  causes increased deposition at the outer bend of the inflow. This can be explained physically: from Figure 5a, the perturbation results in a larger sediment grain size at the inflow, which only the faster velocity at the outer bend can erode. This sediment also gets deposited quickly because of its mass, meaning the overall effect is increased deposition in this area. In the rest of the domain, the perturbation in  $d_{50}$  accentuates the sediment transport patterns already present in the original final bedlevel (see Figure 2), which is a sensible result.

Perturbing  $k_s$  causes increased deposition at the inflow and increased erosion at the outflow and within this trend more deposition at the inner bend and more erosion at the outer bend, as shown in Figure 6b. This has a physical explanation, as increasing the friction in a region decreases the velocity there, leading to increased deposition, with the inverse also true. The different behaviour at the inner and outer bend can be explained by two reasons: (i) from Figure 5b, the friction perturbation is lower at the outer bend, meaning flow is pushed towards this region which leads to increased erosion; (ii) the velocity is naturally faster at the outer bend due to the helical flow effect, and thus is less affected by the friction increase.

Thus, the results in this section demonstrate that our *Thetis*-pyadjoint framework can accurately analyse the sensitivity of our model to uncertain spatially-varying parameters for a complex test case.

## Calibration, inversion and sensitivity analysis for hydro-morphodynamic models



**Figure 5:** Sensitivity of integrated bedlevel to different spatially-varying parameters for the Meander test case using the *Thetis*-pyadjoint framework. A positive value indicates increasing the uncertain values at this location increases the bedlevel change and vice versa for a negative value.

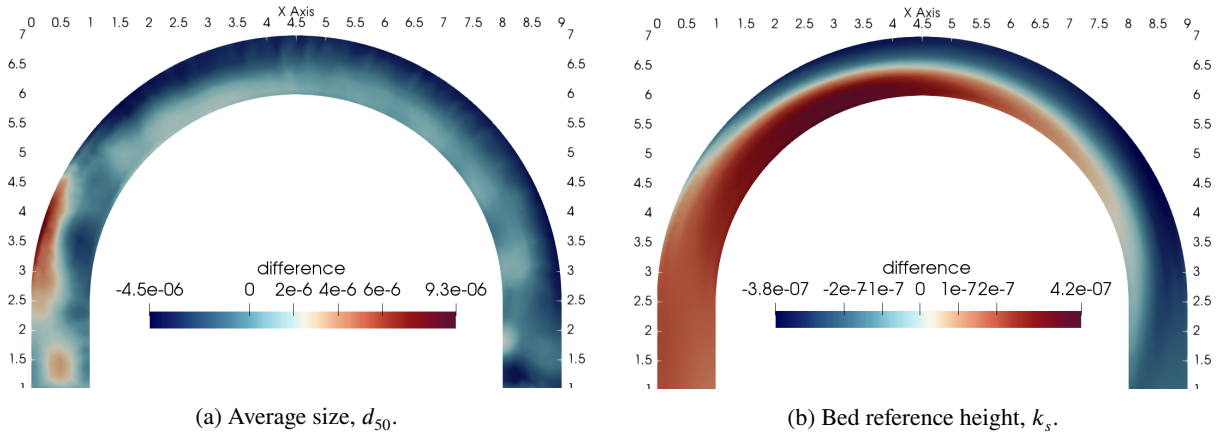


**Figure 6:** Difference between the original and the perturbed final bathymetries as a spatially varying field simulated using *Thetis*, where the perturbed bedlevel is obtained by perturbing the uncertain spatially-varying parameters from their original value in the direction of their derivative, for the Meander test case. Note a positive value indicates more deposition and a negative value more erosion.

## 5. Optimum parameter calibration for a migrating Trench

As discussed in Section 2.1, adjoint methods can also be used to calibrate for uncertain parameters. We illustrate this by considering a migrating trench which has already been verified and validated for our hydro-morphodynamic model in Clare et al. (2021a) and for which experimental data exists in Van Rijn (1980). Throughout this section, unless otherwise stated, we use the set-up of Clare et al. (2021a) with a mesh of  $\Delta x = 0.25$  m and  $\Delta y = 0.2$  m and a morphological acceleration factor,  $m_f$ , of 100.

### 5.1. Dual twin experiment

We first conduct a dual-twin experiment, where the ‘true’ output is generated by a previous model run. Thus, we know the value of the ‘uncertain’ parameter and can verify that our framework can reconstruct it. Given we are not trying to match with experimental data and for reasons of time, the simulation is only run for 5 h instead of the full experimental time of 15 h.

To be consistent between the dual twin experiment and the calibration in Section 5.2, we assume here that the  $z_b^{\text{true}}$  profile is only known at certain locations, as is the case with real world data. Following Saito et al. (2011), we extract the bedlevel at these locations by multiplying the model bedlevel and the ‘true’  $z_b$  by a Gaussian function centred at the experimental data locations,  $x_i$

$$\hat{z}_b(x; x_i) = z_b \times \left( \exp^{-50(x-x_i)^2} \right), \quad (19)$$

where the exponent is scaled by 50 to ensure the base of the Gaussian function is narrow around  $x_i$  and we use our knowledge of the test case to assume no variation in the  $y$ -direction. Thus, the general functional (11) from Section 2.1 becomes

$$J(z_b, m) = \frac{1}{2} \sum_{i=1}^k \frac{\int_{\Omega} |\hat{z}_b^{\text{model}}(x; x_i) - \hat{z}_b^{\text{true}}(x; x_i)|^2 dx}{\int_{\Omega} |\exp^{-50(x-x_i)^2}|^2 dx}, \quad (20)$$

where  $k$  is the number of experimental data points and the Gaussian function has been normalised. The integral over time in (11) is unnecessary because the experimental data only exists at one point in time.

One of the advantages of adjoint methods is that the number of uncertain parameters has almost no effect on the computational cost and therefore here we choose to reconstruct multiple uncertain reference parameters at once. Note that unlike in the previous section, we consider them to be spatially-constant. For our uncertain parameters, we choose  $d_{50}$  and  $k_s$  because they are both key in determining sediment transport rate (see Section 4), the sediment density  $\rho_s$  because it follows that if sediment size is uncertain then sediment density may also be uncertain, and the diffusivity parameter  $\epsilon_s$  because Clare et al. (2021a) show this test case is very sensitive to it. To generate the ‘true’ output, we use the values  $\rho_s = 2000 \text{ kg m}^{-3}$ ,  $d_{50} = 2 \times 10^{-4} \text{ m}$ ,  $k_s = 0.01 \text{ m}$  and  $\epsilon_s = 0.01 \text{ m}^2 \text{ s}^{-1}$ . We then use  $\rho_s = 2650 \text{ kg m}^{-3}$ ,  $d_{50} = 1.6 \times 10^{-4} \text{ m}$ ,  $k_s = 0.025 \text{ m}$  and  $\epsilon_s = 0.15 \text{ m}^2 \text{ s}^{-1}$  as the initial guesses to start the optimisation algorithm. Note, because these four parameters have different orders of magnitude, to ensure the optimisation algorithm works, we scale them by multiplying them by one over their order of magnitude so that the scaled parameters all have order of magnitude of 1. Naturally, within the forward model, these are then re-scaled to ensure physically correct results.

Figure 7a shows that the output functional (20) decreases at each iteration of the optimisation algorithm (10). This results in a general error reduction in the scaled  $\rho_s$ ,  $d_{50}$ ,  $k_s$  and  $\epsilon_s$  shown in Figure 7b. However, this reduction is not always smooth most likely because, at some iterations, minimising the functional causes a decrease in some parameters’ error but an increase in others. A better metric to look at is the total error (*i.e.* the sum of the error from the four individual parameters) which does decrease more uniformly. Furthermore, at the final iteration, the error between the reconstructed and actual scaled values has an approximate order of magnitude of  $10^{-3}$  or better for all four parameters, corresponding to an unscaled order of magnitude error of approximately  $1 \times 10^{-2} \text{ kg m}^{-3}$  for  $\rho_s$ ,  $1 \times 10^{-9} \text{ m}$  for  $d_{50}$ ,  $1 \times 10^{-5} \text{ m}$  for  $k_s$  and  $1 \times 10^{-5} \text{ m}^2 \text{ s}^{-1}$  for  $\epsilon_s$ . A smaller error could be achieved by reducing the tolerance in the optimisation algorithm, but these errors are already much smaller than mesh or model error. Thus, they demonstrate that adjoint methods can be used to calibrate for multiple spatially-constant parameters in the hydro-morphodynamic model in one simulation.

## 5.2. Calibration of parameters for a laboratory test case

Following the verification of our adjoint framework, we can now use the same method to perform uncertain parameter calibration with experimental data. We use the same migrating trench test case set-up as in Section 5.1 but now run the simulation for the full experimental time (15 h) and set the true values in (20) to be the experimental data in Van Rijn (1980).

Clare et al. (2021a) conduct parameter calibration for this test case for  $\epsilon_s$  using trial-and-error, and estimate an optimum value of  $\epsilon_s = 0.15 \text{ m}^2 \text{ s}^{-1}$ . Therefore, as a first test,  $\epsilon_s$  is considered uncertain. Figure 8a shows the functional decreases with each iteration, and Figure 8b shows how this leads to the convergence of  $\epsilon_s$  to an optimal value of  $0.183 \text{ m}^2 \text{ s}^{-1}$ , which is close to the value estimated in Clare et al. (2021a), giving further confidence in our adjoint framework.

Given this result, we now calibrate for the optimum values of the four uncertain parameters  $\rho_s$ ,  $d_{50}$ ,  $k_s$  and  $\epsilon_s$ , as in Section 5.1, scaling the parameters so that they all have an approximate order of magnitude of 1. Furthermore, to ensure the optimum values obtained are physical and do not blow up during the optimisation, we add Tikhonov

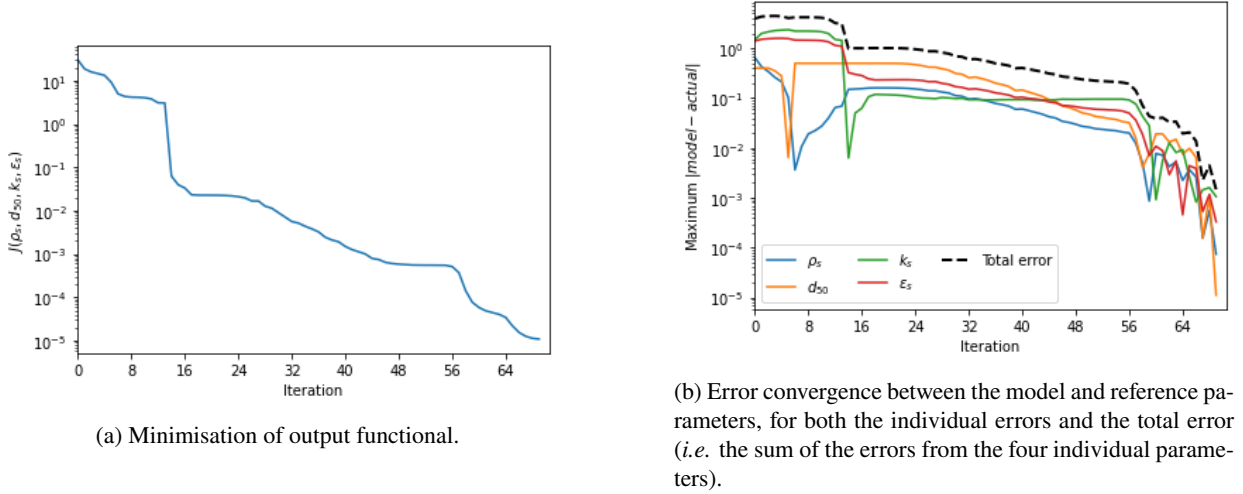


**Figure 7:** Using adjoint methods to find reference sediment parameters  $d_{50}$ ,  $\rho_s$ ,  $k_s$  and  $\epsilon_s$  for the Trench test case.

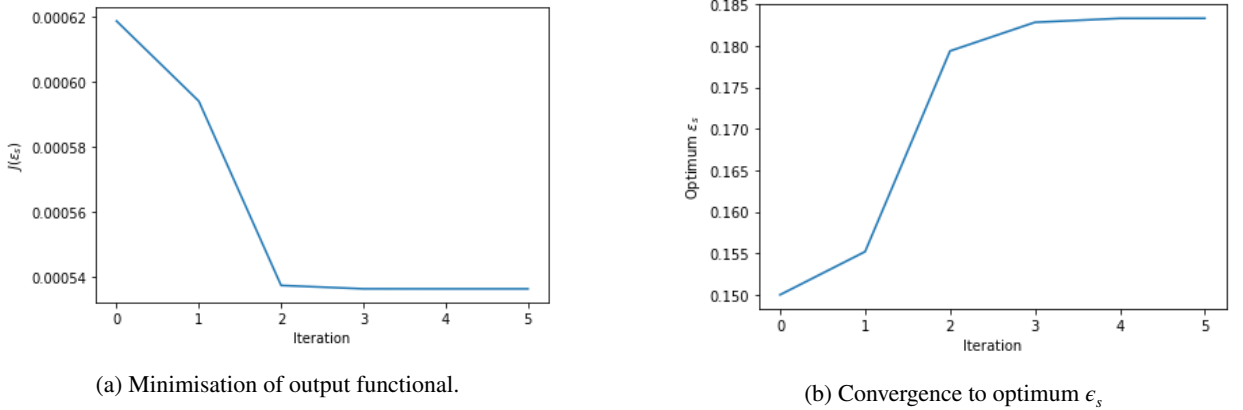


**Figure 8:** Using adjoint methods to find optimum diffusivity parameter,  $\epsilon_s$ , for the Trench test case.

regularisation (20):

$$J(z_b, \mathbf{m}) = \alpha \sum_{i=1}^k \frac{\int_{\Omega} |\hat{z}_b^{\text{model}}(x; x_i) - \hat{z}_b^{\text{true}}(x; x_i)|^2 dx}{\int_{\Omega} |\exp^{-50(x-x_i)^2}|^2 dx} + \sum_{i=1}^{N_{\text{in}}} \beta_i \int_{\Omega} |m_i|^2 dx, \quad (21)$$

where the ‘true’ value is taken to be the experimental data in Van Rijn (1980),  $\alpha = 1000$ , and  $\beta_i$  is equal to  $10^{-4}$  for  $\rho_s$ ,  $d_{50}$  and  $k_s$ , and equal to  $5 \times 10^{-5}$  for  $\epsilon_s$ , because Clare et al. (2021a) shows  $\epsilon_s$  has a large impact on the final result. For the initial guesses for the optimisation algorithm, we use the original parameter values for this test case from Clare et al. (2021a).

Figure 9a shows that the functional value decreases with each iteration and Figure 9b shows that this leads to the convergence of all four parameters to optimal values. The parameters shown in the figure are the scaled ones and therefore the actual optimum value of  $\rho_s$  is  $2511 \text{ kg m}^{-3}$ ; of  $d_{50}$  is  $1.99 \times 10^{-4} \text{ m}$ ; of  $k_s$  is  $0.0341 \text{ m}$  and of  $\epsilon_s$  is  $0.321 \text{ m}^2 \text{ s}^{-1}$ . Note the optimum  $\epsilon_s$  value here is much greater than its value when we optimised for  $\epsilon_s$  on its own, showing a clear difference in results if parameters are optimised individually or in a group. To summarise, the optimum

sediment is less dense, larger, erodes less easily and diffuses at a greater rate than assumed in the original simulation.

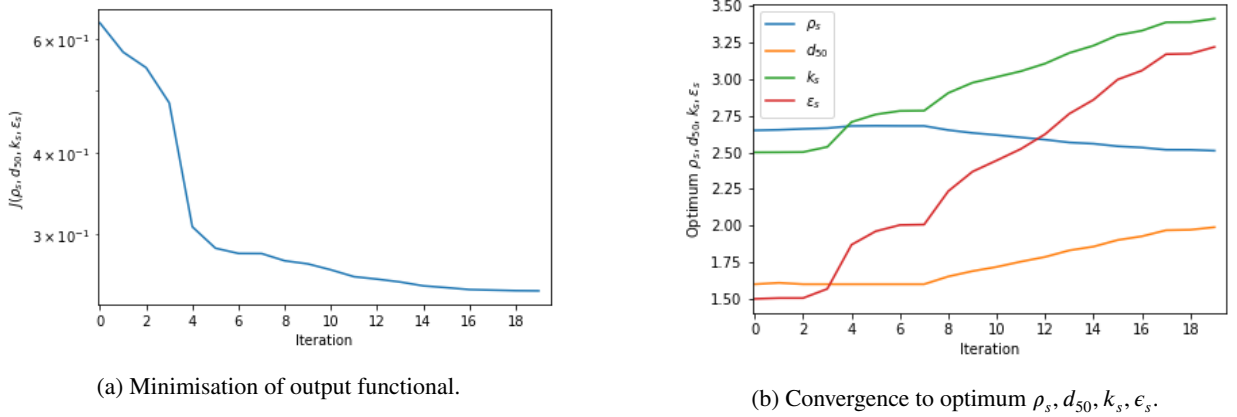


**Figure 9:** Using adjoint methods to find optimum sediment density,  $\rho_s$ ; sediment size  $d_{50}$ ; bed reference height,  $k_s$ ; and diffusivity parameter  $\epsilon_s$  for the Trench test case.

Figure 10a compares the final bedlevel obtained using either all four optimum parameters, just the optimum diffusivity parameter, or the original values from Villaret et al. (2016). It shows that  $\epsilon_s$  has the largest impact on accuracy, but that using optimum choices for all four parameters improves the accuracy further, in particular the gradient of the slope. In order to test the robustness of these optimum parameters we re-run the test case using a coarser mesh of  $\Delta x = 1$  m (compared to the  $\Delta x = 0.25$  m mesh used originally), although the initial trench profile is not well defined for this coarser mesh. Figure 10b shows the accuracy improvements with the coarser mesh are similar to before, including the improved gradient from using four optimal parameters. This suggests these optimum parameters are not resolution dependent and thus that our adjoint framework can accurately calibrate multiple uncertain scalar parameters in this test case.

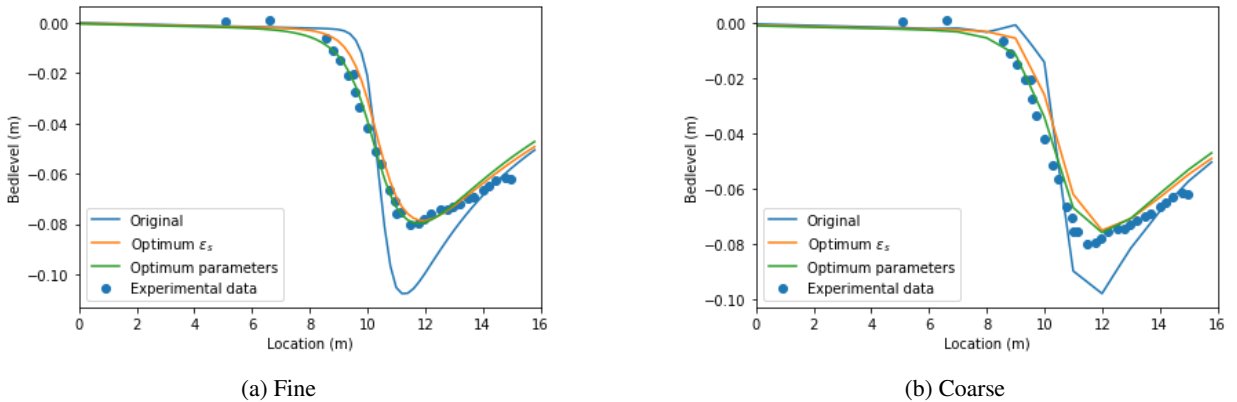


**Figure 10:** Final bedlevel on both a fine and coarse mesh as a result of using the original parameters from Villaret et al. (2016); the optimum  $\epsilon_s$  parameter; and the optimum  $\rho_s, d_{50}, k_s$  and  $\epsilon_s$  parameters for the Trench test case. For comparison the experimental data is also shown demonstrating the accuracy improvements from using the values obtained using the adjoint method.

## 6. Tsunami inversion

As our final test case, we consider a tsunami-like event. Tsunami events are often difficult to simulate due to the large array of uncertain parameters, especially for historical scenarios where the only record is in the form of sediment

deposits (e.g. Tang et al., 2018; Dourado et al., 2021). These uncertain parameters are often estimated by using educated guesses in a forward model and adjusting their value accordingly by comparing the model results with the data (see e.g. Dourado et al., 2021). A more sophisticated approach is to use tsunami inversion models such as TSUNFLIND (see Tang and Weiss, 2015) which has been coupled with statistical methods in Tang et al. (2018). However, these inversion models do not have the full capabilities of standard forward models, for example TSUNFLIND cannot model bedload transport. Tsunami events are therefore an ideal scenario on which to apply our hydro-morphodynamic adjoint framework. For our test case, we consider the experiment in Kobayashi and Lawrence (2004), where a tsunami-like solitary wave repeatedly breaks over a sloping beach.

### 6.1. Forward model set-up and results

For this test case not all of the domain is wet, hence we use the wetting-and-drying version of the hydro-morphodynamic model detailed in Section 3.1. The beach slope also requires the use of the sediment slide mechanism (detailed in Clare et al. (2021b)).

Following Kobayashi and Lawrence (2004), the wave is simulated by imposing the following free surface elevation boundary condition at the open boundary

$$\eta(t) = H_{\text{wave}} \operatorname{sech}^2 \left( \sqrt{\frac{3H_{\text{wave}}}{4h}} \frac{\sqrt{g(H_{\text{wave}} + h)}}{h} (t - t_{\text{max}}) \right) + \eta_{\text{down}}, \quad (22)$$

which causes a tsunami-like solitary wave to travel into the domain. Here  $H_{\text{wave}}$  is the average wave height,  $h$  the still water depth,  $t_{\text{max}}$  the arrival time of the wave crest at the open boundary and  $\eta_{\text{down}}$  the initial decrease of the elevation at the beginning of the simulation (also the initial elevation in the domain). Our model cannot currently simulate shoaling and breaking waves and thus a relatively high viscosity value of  $0.8 \text{ m}^2\text{s}^{-1}$  is used in the hydrodynamics to dissipate energy. This is standard practice, for example Li and Huang (2013) view viscosity as a model calibration parameter for energy dissipation, rather than a physical parameter.

The remaining parameters, taken from Kobayashi and Lawrence (2004) and Li and Huang (2013), are summarised in Table 1. Note Li and Huang (2013) run the simulation for 40 s with  $t_{\text{max}} = 23.9$  s for each solitary wave, but the system is stationary for the first 20 s. Therefore we only run our model simulation for 20 s with  $t_{\text{max}} = 3.9$  s for each solitary wave. Furthermore, we found that our final model results are fairly insensitive to the morphological acceleration factor,  $m_f$ . Hence, here we set  $m_f$  equal to four, meaning we only need to model two solitary waves to simulate the bed changes caused by the eight waves in the experiment.

Figure 11 shows there is good agreement between our forward model results and the experimental data obtained in Kobayashi and Lawrence (2004). For comparison, this agreement is more than competitive with that shown between the results and the experimental data for a similar test case in Kazhyken et al. (2021) which uses a dispersive wave model. Thus, our forward model is validated for this test case and we proceed to using the adjoint framework.

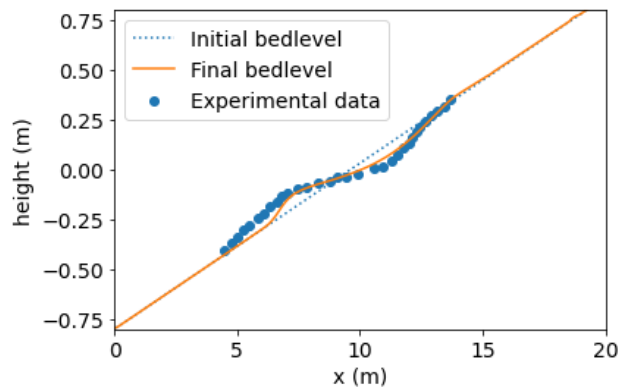


**Figure 11:** Final bedlevel simulated by *Thetis* compared to experimental data from Kobayashi and Lawrence (2004) after eight solitary waves for the Tsunami test case.

**Table 1**

Parameter values for the Tsunami test case.

Variable Name	Variable Value
Length in $x$ -direction	30 m
Length in $y$ -direction	4 m
Bed slope	1/12
$\Delta x = \Delta y$	0.2 m
dt	0.05 s
Morphological simulation time	20 s $\times$ 2
Morphological acceleration factor	4 (thus 2 waves only)
Median particle size ( $d_{50}$ )	$1.8 \times 10^{-4}$ m
Sediment density ( $\rho_s$ )	2650 kg m $^{-3}$
Water density ( $\rho_f$ )	1000 kg m $^{-3}$
Bed sediment porosity ( $p'$ )	0.4
Diffusivity ( $\epsilon_s$ )	1 m $^2$ s $^{-1}$
Chezy friction coefficient ( $n$ )	65 m $^{1/2}$ s $^{-1}$
Angle of repose	22 $^\circ$
Wetting-and-drying parameter	1/30 m
Norm smoother parameter ( $\beta$ )	1/60 m s $^{-1}$
$H_{\text{wave}}$	0.216 m
h	0.18 m
$\eta_{\text{down}}$	-0.0025 m
$t_{\text{max}}$	3.9 s

## 6.2. Reconstructing reference wave from sediment deposits

As discussed in Section 1, the adjoint method is ideally suited to cases where there are multiple uncertain parameters. In this section, we consider the inflow tsunami-like wave boundary condition to be the uncertain time-varying spatially-constant parameter, and use a dual twin experiment to verify our adjoint framework's ability to reconstruct it. For the dual twin, the 'true' data is the bedlevel generated by the reference wave (22) at every timestep. Given we are not matching with experimental data and for reasons of time, here we only run one wave in our simulation but still use a morphological acceleration factor of four, meaning this is equivalent to simulating four waves. For our initial guess for the optimisation algorithm, we assume the wave was caused by a sudden rupture in the Earth's crust causing a discontinuous wave profile

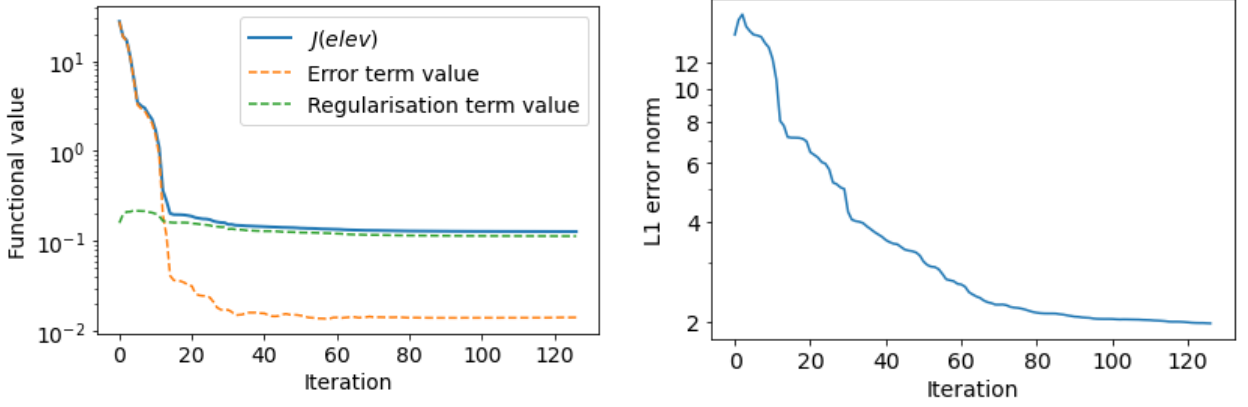
$$\eta_{\text{initial}}(t) = \begin{cases} 0.05 \text{ m} & t < 7.5 \text{ s}, \\ 0 \text{ m} & \text{otherwise,} \end{cases} \quad (23)$$

as shown in Figure 13. Note, only the first 10 s of the wave are considered to be uncertain because we know the 'true' free surface perturbation is only non-zero at the boundary between 2 s and 6 s, so considering the whole time region is unnecessary.

For the output functional, we use (21) with a time integral,  $\beta_i = 10^{-4}$  in the regularisation term and  $\alpha = 1$  in the error term, and centre the Gaussian functions (19) at the experimental data locations in Kobayashi and Lawrence (2004). Figure 12a shows that the output functional, and the error and regularisation terms within it, decrease as the number of iterations of the optimisation algorithm increases. Notably, even when the value of the regularisation term is larger than that of the error term, the latter is still decreasing. This minimisation of the functional results in the convergence of the L1 error norm between the reference input and model input waves, as shown in Figure 12b. The effect of the minimisation on the model wave itself is shown in Figure 13, revealing the model wave has the correct general shape already by iteration 50. Finally, the figure shows the final iteration approximates the reference wave very well, meaning our adjoint framework is capable of reconstructing an input solitary wave from sediment deposits.

## 6.3. Finding the optimum wave from sediment deposits

We now consider the inversion of the wave from the experimental sediment deposit data in Kobayashi and Lawrence (2004). This data only exists for the final bedlevel and thus the problem would be ill-posed without regularisation terms



(a) Minimisation of the output functional. The convergence of the error term and the regularisation term in (11) are also shown. (b) Convergence of the L1 error norm between the model wave and the reference tsunami-like wave.

**Figure 12:** Using adjoint methods to reconstruct the reference wave for the dual-twin experiment of the Tsunami test case.

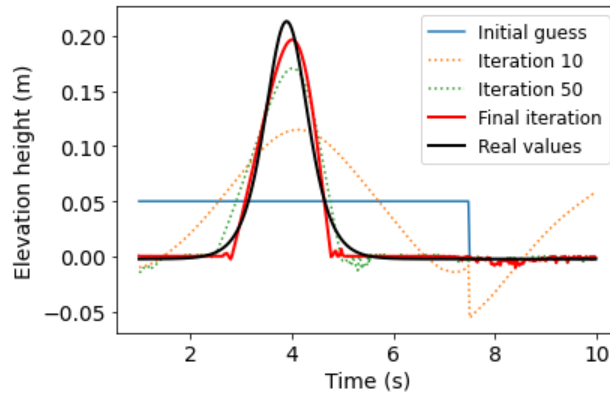


**Figure 13:** Comparing the model wave at a series of different iterations of the optimisation algorithm (including the final iteration) with the reference wave for the dual-twin experiment in the tsunami test case.

in our output functional. Moreover, we add a regularisation term to enforce continuity in the wave because using the same output functional as in Section 6.2 was observed to result in large jumps in waveheight. Therefore, the output functional is

$$\begin{aligned}
 J(z_b, \mathbf{m}) = & \alpha \sum_{i=1}^k \frac{\int_{\Omega} |\hat{z}_b^{\text{model}}(x; x_i) - \hat{z}_b^{\text{true}}(x; x_i)|^2 dx}{\int_{\Omega} |\exp^{-50(x-x_i)^2}|^2 dx} + \sum_{i=1}^{N_{\text{in}}} \beta_i \int_{\Omega} |m_i|^2 dx \\
 & + \sum_{i=2}^{N_{\text{in}}} \gamma_i \int_{\Omega} |m_i - m_{i-1}|^2 dx,
 \end{aligned} \tag{24}$$

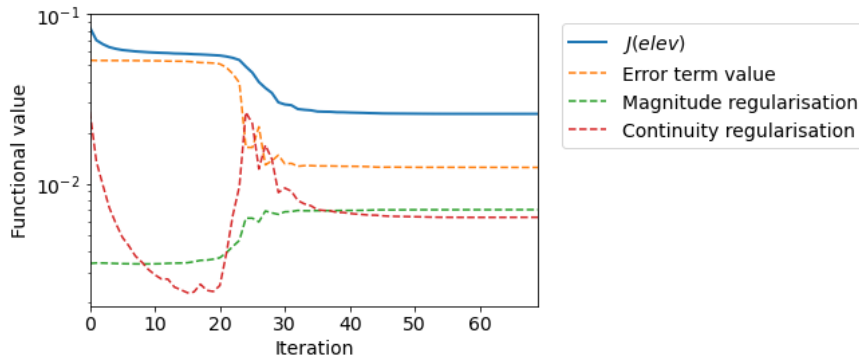
where  $m_i$  represents the input wave at time  $t_i$ , the scalar parameters are  $\alpha = 1$ ,  $\beta_i = 5 \times 10^{-6}$  and  $\gamma_i = 5 \times 10^{-2}$ , and the Gaussian functions are centered at the experimental data locations.

To ensure stability, we enforce the wave elevation to be 0 m at both the start and end of the simulation, and only consider the wave to be uncertain during the middle of the simulation, where we initialise the optimisation algorithm using an initial elevation of 0.05 m (see Figure 15a). This replicates the initial guess of a discontinuous wave profile

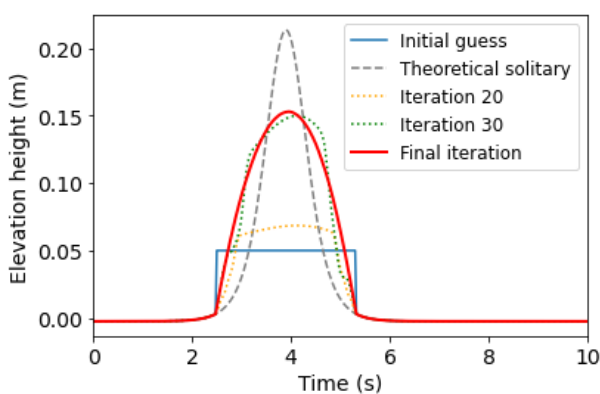
from Section 6.2. All model parameters are as described in Section 6.1 and we simulate two solitary waves with a morphological acceleration factor of four because we are comparing against real data.

Figure 14 shows the output functional (24) decreases as the number of iterations of the optimisation algorithm increases, causing the value of the error term in (24) to decrease. The trend in the magnitude and continuity regularisation terms is less uniform, but can be loosely interpreted as follows: for the first 20 iterations the optimisation algorithm minimises the continuity term, from 20 to 30 iterations it minimises the error term at the expense of the magnitude term and after iteration 30 it again minimises the continuity term. This interpretation is confirmed by the differences between iterations 20, 30 and the final one in Figure 15a.

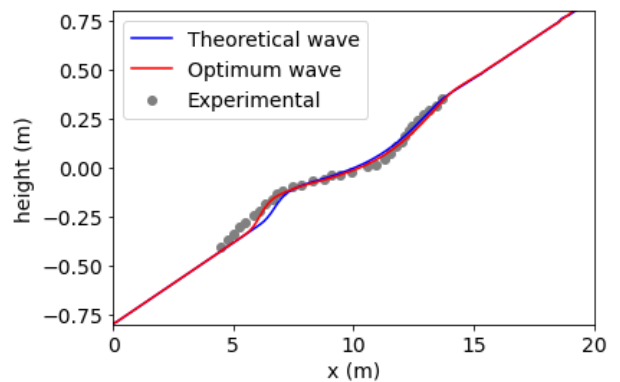
Figure 15a compares the optimum wave found in this section with the theoretical solitary wave (22) that Kobayashi and Lawrence (2004) used to describe the incoming wave observed in their experiment. It shows our optimum wave has a wider base and a smaller amplitude than (22). Consequently, Figure 15b shows the simulated bedlevel from the optimum wave has very good agreement with the experimental data and this agreement is much better than that with the theoretical wave, particularly in the area of deposition between 5 m and 10 m. Therefore, our adjoint framework can be used to invert accurately for tsunami-like waves from final bedlevel sediment deposits, which is a very promising result.



**Figure 14:** Minimisation of the output functional as the number of iterations increases for the optimum wave for the Tsunami test case. The convergence of the error term and the change in the magnitude and continuity regularisation terms in (24) are also shown separately.



(a) Optimum wave compared to the wave at selected intermediary iterations and the theoretical solitary wave (22).



(b) Comparing the final bedlevel obtained using the optimum wave with that from the experiment and from using the theoretical solitary wave (22).

**Figure 15:** Comparing the optimum wave found by our adjoint framework with the theoretical solitary wave (22) that Kobayashi and Lawrence (2004) used to describe the incoming wave observed in their experiment, for the Tsunami test case.

## 7. Conclusion

In this work, we have developed the first freely available and fully flexible adjoint hydro-morphodynamic framework. By fully flexible we mean that the use of *pyadjoint* allows us to assess any parameter uncertainty in the hydro-morphodynamic model with respect to any output functional. Hence, we have shown that our framework can perform calibration, inversion or sensitivity analysis of multiple uncertain parameters in a single model run and have verified these capabilities using dual-twin experiments. Moreover, we showed that these inversion and calibration capabilities can produce physically-sensible results with experimental data and that the optimum parameters obtained using these methods result in more accurate final bedlevels. Notably, we showed that our approach is capable of reconstructing the shape and magnitude of incoming waves from the resulting sediment deposits. The next stage of our work will be to apply our approach to historical tsunami sediment deposits to invert for the tsunami wave. This will contribute to a better understanding of historical tsunami events and help mitigate the impacts of future events.

Moreover, as the dimension of the uncertain parameters has little effect on the computational cost, our framework is capable of addressing the uncertainty of spatially-varying parameters. Thus, we showed that a single run of our adjoint framework can determine where changing the friction and sediment size causes the greatest bed level change, for example. Obtaining this type of uncertainty information using other methods, such as Monte Carlo or via the tangent linear approach, is either impractical or much more computationally expensive. Therefore, the knowledge gained through our adjoint framework can be invaluable to a variety of users and stakeholders in understanding and mitigating the impacts of coastal and fluvial hazards.

## 8. Acknowledgements

MCAC's work was funded through the EPSRC CDT in Mathematics for Planet Earth and grant EP/R512540/1. SCK, CJC and MDP acknowledge the support of EPSRC through the grants EP/L016613/1, EP/R007470/1 and EP/R029423/1.

## Code availability

The relevant code for the adjoint hydro-morphodynamic framework presented in this work is written in Python and can be found at [https://github.com/mc4117/adjoint\\_hydro\\_morphodynamic](https://github.com/mc4117/adjoint_hydro_morphodynamic). Zenodo releases have been made for all software requirements for this code and these can be found at the following DOIS: Firedrake <https://doi.org/10.5281/zenodo.5105703>; Thetis <https://doi.org/10.5281/zenodo.5105623>; pyadjoint <https://doi.org/10.5281/zenodo.5105785>.

## References

- Chen, H., Cao, A., Zhang, J., Miao, C., Lv, X., 2014. Estimation of spatially varying open boundary conditions for anumerical internal tidal model with adjoint method. *Mathematics and Computers in Simulation* 97, 14–38.
- Clare, M.C.A., Percival, J.R., Angeloudis, A., Cotter, C.J., Piggott, M.D., 2021a. Hydro-morphodynamics 2D modelling using a discontinuous Galerkin discretisation. *Computers & Geosciences* 146.
- Clare, M.C.A., Wallwork, J., Kramer, S.C., Weller, H., Cotter, C.J., Piggott, M., 2021b. Multi-scale hydro-morphodynamic modelling using mesh movement methods .
- Dalledonne, G., Kopmann, R., Riehme, J., Naumann, U., 2017. Uncertainty analysis approximation for non-linear processes using Telemac-AD, in: *Proceedings of the XXIVth TELEMAT-MASCARET User Conference*, 17 to 20 October 2017, Graz University of Technology, Austria, Graz University of Technology, Graz, pp. 65–71. URL: <https://hdl.handle.net/20.500.11970/104486>.
- Dissanayake, P., Brown, J., Karunarathna, H., 2014. Modelling storm-induced beach/dune evolution: Sefton coast, Liverpool Bay, UK. *Marine Geology* 357, 225–242. doi:10.1016/J.MARGEO.2014.07.013.
- Dourado, F., Costa, P., La Selle, S., Andrade, C., Silva, A., Bosnic, I., Gelfenbaum, G., 2021. Can modeling the geologic record contribute to constraining the tectonic source of the 1755 ce great lisbon earthquake? *Earth and Space Science* 8, e2020EA001109.
- Engl, H.W., Hanke, M., Neubauer, A., 1996. Regularization of inverse problems. volume 375. Springer Science & Business Media.
- Farrell, P.E., Ham, D.A., Funke, S.W., Rognes, M.E., 2013. Automated derivation of the adjoint of high-level transient finite element programs. *SIAM Journal on Scientific Computing* 35, 369–393.
- Firedrake Project, 2021. Fix split pull request #1609. URL: <https://github.com/firedrakeproject/firedrake/pull/1609/files>.
- Funke, S., Farrell, P., Piggott, M., 2017. Reconstructing wave profiles from inundation data. *Computer Methods in Applied Mechanics and Engineering* 322, 167–186.
- Funke, S.W., 2012. The automation of PDE-constrained optimisation and its applications. Ph.D. thesis. Imperial College London. doi:10.13140/2.1.3688.0967.
- Harris, D.L., Rovere, A., Casella, E., Power, H., Canavesio, R., Collin, A., Pomeroy, A., Webster, J.M., Parravicini, V., 2018. Coral reef structural complexity provides important coastal protection from waves under rising sea levels. *Science Advances* 4.

- Heemink, A.W., Mouthaan, E.E.A., Roest, M.R.T., Vollebregt, E.A.H., Robaczewska, K.B., Verlaan, M., 2002. Inverse 3D shallow water flow modelling of the continental shelf. *Continental Shelf Research* 22, 465–484.
- Hervouet, J.M., 1999. TELEMAC, a hydroinformatic system. *Houille Blanche-revue Internationale De L Eau* 54, 21–28. doi:10.1051/1hb/1999029.
- Hieu, M.T., Nowak, W., Kopmann, R., 2006. Using algorithmic differentiation for uncertainty analysis, in: Moulinec, C., Emerson, D. (Eds.), XXII TELEMAC-MASCARET Technical User Conference October 15-16, Warrington. pp. 52–58. URL: <https://hdl.handle.net/20.500.11970/104343>.
- Jaffe, B.E., Goto, K., Sugawara, D., Gelfenbaum, G., La Selle, S., 2016. Uncertainty in tsunami sediment transport modeling. *Journal of Disaster Research* 11, 647–661. doi:10.20965/jdr.2016.p0647.
- Jones, E., Oliphant, T., Peterson, P., 2001. Scipy: Open source scientific tools for python .
- Kärnä, T., de Brye, B., Gourgue, O., Lambrechts, J., Comblen, R., Legat, V., Deleersnijder, E., 2011. A fully implicit wetting&Amdrying method for DG-FEM shallow water models, with an application to the Scheldt Estuary. *Computer Methods in Applied Mechanics and Engineering* 200, 509–524.
- Kärnä, T., Kramer, S., Mitchell, L., Ham, D., Piggott, M., Baptista, A., 2018. Thetis coastal ocean model: discontinuous Galerkin discretization for the three-dimensional hydrostatic equations. *Geoscientific Model Development* 11, 4359–4382.
- Kazhyken, K., Videman, J., Dawson, C., 2021. Discontinuous Galerkin methods for a dispersive wave hydro-sediment-morphodynamic model. *Computer Methods in Applied Mechanics and Engineering* 377, 113684. URL: <https://doi.org/10.1016/j.cma.2021.113684>, doi:10.1016/j.cma.2021.113684, arXiv:2010.06167.
- Kobayashi, N., Lawrence, A.R., 2004. Cross-shore sediment transport under breaking solitary waves. *Journal of Geophysical Research: Oceans* 109. doi:10.1029/2003jc002084.
- Kopmann, R., Merkel, U., Riehme, J., 2012. Using Reliability Analysis in Morphodynamic Simulation with TELEMAC-2D / SISYPHE, in: XIXth TELEMAC-MASCARET User Conference, Oxford, UK, October 18-19, 2012., HR Wallingford, Wallingford, Oxfordshire, UK. pp. 119–125.
- Li, L., Huang, Z., 2013. Modeling the change of beach profile under tsunami waves: A comparison of selected sediment transport models. *Journal of Earthquake and Tsunami* 7. doi:10.1142/S1793431113500012.
- Merkel, U., Riehme, J., Naumann, U., 2013. Reverse Engineering of Initial & Boundary Conditions with TELEMAC and Algorithmic Differentiation, in: Kopmann, R., Goll, A. (Eds.), XXth TELEMAC-MASCARET. User Conference 2013., Karlsruhe. pp. 25–30. URL: <https://hdl.handle.net/20.500.11970/100423>.
- Merkel, U., Riehme, J., Naumann, U., 2016. River flow analysis with adjoints - An efficient, universal methodology to quantify spatial interactions and sensitivities, in: Erpicum, S., Dewals, B., Archambeau, P., Piroton, M. (Eds.), Sustainable Hydraulics in the Era of Global Change. Taylor & Francis Group, London, UK, pp. 538–544.
- Naumann, U., Riehme, J., 2008. Sensitivity Analysis in Sisyphe with the AD-Enabled NAGWare Fortran Compiler. Technical Report. Department of Computer Science, RWTH Aachen University. Aachen, Germany. URL: <https://www.researchgate.net/publication/267305598>.
- Parkinson, S.D., Funke, S.W., Hill, J., Piggott, M.D., Allison, P.A., 2017. Application of the adjoint approach to optimise the initial conditions of a turbidity current with the AdjointTurbidity 1.0 model. *Geoscientific Model Development* 10, 1051–1068.
- Rathgeber, F., Ham, D.A., Mitchell, L., Lange, M., Luporini, F., McRae, A.T., Bercea, G., Markall, G., Kelly, P.H., 2017. Firedrake: automating the finite element method by composing abstractions. *ACM Transactions on Mathematical Software (TOMS)* 43, 24.
- Riehme, J., Kopmann, R., Naumann, U., 2010. Uncertainty quantification based on forward sensitivity analysis in Sisyphe, in: Pereira, J.C.F., Sequeira, A. (Eds.), V European Conference on Computational Fluid Dynamics, Lisbon, Portugal.
- Saito, T., Ito, Y., Inazu, D., Hino, R., 2011. Tsunami source of the 2011 tohoku-oki earthquake, japan: Inversion analysis based on dispersive tsunami simulations. *Geophysical Research Letters* 38.
- Tang, H., Wang, J., Weiss, R., Xiao, H., 2018. TSUFLIND-EnKF: Inversion of tsunami flow depth and flow speed from deposits with quantified uncertainties. *Marine Geology* 396, 16–25.
- Tang, H., Weiss, R., 2015. A model for tsunami flow inversion from deposits (tsuflind). *Marine geology* 370, 55–62.
- Unguendoli, S., 2018. Propagation of uncertainty across modeling chains to evaluate hydraulic vulnerability in coastal areas. Ph.D. thesis. Università di Bologna, Bologna, Italy. URL: [http://amsdottorato.unibo.it/8599/1/Unguendoli\\_{\\_}Silvia\\_{\\_}Tesi.pdf](http://amsdottorato.unibo.it/8599/1/Unguendoli_{_}Silvia_{_}Tesi.pdf).
- Van Rijn, L.C., 1980. Storm surge barrier Oosterschelde-computation of siltation in dredged trenches: Semi-empirical model for the flow in dredged trenches. Deltares, Delft, The Netherlands.
- Villaret, C., Kopmann, R., Wyncoll, D., Riehme, J., Merkel, U., Naumann, U., 2016. First-order uncertainty analysis using Algorithmic Differentiation of morphodynamic models. *Computers & geosciences* 90, 144–151.
- Warder, S.C., Horsburgh, K.J., Piggott, M.D., 2021. Adjoint-based sensitivity analysis for a numerical storm surge model. *Ocean Modelling* , 101766.
- Yen, C.I., Lee, K.T., 1995. Bed topography and sediment sorting in channel bend with unsteady flow. *Journal of Hydraulic Engineering* 121, 591–599.